Programmable Multifunctional Plasmonic Waveguide System based on Coding Metamaterials and Inverse Design

Yihang Dan, Tian Zhang,* Jian Dai, and Kun Xu

State Key Laboratory of Information Photonics and Optical Communications, Beijing University of Posts and Telecommunications, Beijing

E-mail: ztian@bupt.edu.cn

Abstract

In this article, we propose a programmable plasmonic waveguide system (PPWS) to achieve several different functions based on metal coding metamaterials (MCMs) and inverse design technology. There is no need to spend much time on considering the relation between the function and the structure because the MCMs in the PPWS are reprogrammable. In order to demonstrate the effectiveness of the PPWS, we utilize it to achieve several filtering functions, including bandstop and bandpass filters. The simulation results exhibit that the performance of filters is improved based on genetic algorithm, particle swarm optimization, multi-traversal direct-binary search and simulated annealing. Especially, the bandwidth and quality factor for the narrow-band filter can reach 6.5 nm and 200.5. In addition to the simple filtering functions, some relatively complex transmission characteristics can be obtained by using the PPWS, such as plasmon-induced transparency-like effects. In conclusion, genetic algorithm is considered as the most efficient inverse design method for our system due to its less optimization time and stable performance. In comparison with the previous works,

our proposed PPWS not only provides a general framework for obtaining an effective, flexible and compact plasmonic device but also shows the applications of inverse design on photonics devices.

Keywords

Plasmonic devices, inverse design, optimization, plasmon-induced transparency

1 Introduction

Surface plasmon polaritons (SPPs) are especial electromagnetic waves which occur and propagate at the interface of metal and dielectric and they carry energy and information overcoming the diffraction limit.[1] The appearance of SPPs provides a new way to manipulate light at the nanoscale so it is considered to be the most potential way to realize highly integrated optical system in the future.[2] Since SPPs are discovered, researchers have studied different ways to excite SPPs, such as grating excitation,[3] prism coupling,[4,5] waveguide mode coupling,[6] end-fire coupling[7] and local excitation.[8] The transmission of SPPs usually depends on special waveguide systems, for example metal-dielectric-metal (MDM) waveguide,[9] insulator-metal-insulator waveguide,[10] hybrid waveguide[11] and so on. Due to their compact footprint and easy integration, MDM waveguide systems have been widely applied in plasmonic filters,[12,13] splitters,[14,15] optical switches,[16] modulators,[16–18] absorbers,[19] sensors,[20] couplers,[21,22] logic gates[23] and so on. However, in order to realize different functions, researchers often spend much time on searching for and designing the nano-resonators with different shapes.[24–26] For example, the plasmon-induced transparency (PIT) effect,[27,28] which has applications in refractive index sensors and slow light, is a hot spot in the field of SPPs. In order to achieve the PIT effects in the transmission spectrum, various structures of waveguide systems with different resonators have been proposed, such as ring resonators,[29] stub resonators,[30] T-shaped resonators,[31] H-shaped resonators,[32] rectangular resonators,[33]

side-coupled multiple resonators[34–37] and so on. Obviously, it is cumbersome to construct different resonators for a special purpose. It is expected to improve the design efficiency of photonics devices if there exists a general framework, which can realize multiple functions and avoid repetitive design works. It has been demonstrated that the coding metamaterials, which consist of two types of unit cells, can provide a flexible and controllable platform by using a field-programmable gate array.[38] The coding metamaterials are effectively designed to achieve high-performance and easily integrated photonics devices based on the inverse design technology.[39–42] However, it should be noted that the above waveguide systems generally include dielectric coding metamaterials. There are few plasmonic waveguide systems having programmable metal coding metamaterials (MCMs) to obtain multi-functions in a general framework.

The inverse design technology based on optimization algorithms, has been used to search for the appropriate distributions and structure parameter of the MCMs. In general, there are three main ways to implement the inverse design of photonics devices: gradient based methods, gradient free methods and model-based methods.[43] As a representative method of thegradient based methods, adjoint variable method (AVM) can optimize for the linear and nonlinear optical devices, but it needs physical background to derive the gradient of objective function.[44] Model based methods, such as artificial neural networks (ANNs) and random forests, are also used for the inverse design of photonics devices.[45] However, a lot of original data and labels are required to train the model which constructs the physical relationship between the structure parameters and corresponding optical responses. The optimization performance is highly dependent on the effect of pre-training model.[46] In comparison to the model-based methods, the gradient free methods, including search strategy and evolution strategy, are simple and effective as they directly search for the optimal solution by iteration and evolution strategies. Genetic algorithm (GA) and particle swarm optimization (PSO) are two representative evolution algorithms, which are inspired by the genetic inheritance and group cooperation.[47,48] Although GA and PSO have been widely applied in the optimization

and design of photonic devices,[49–56] they are easy to converge too early and fall into local optimal solution in sometimes. Moreover, simulated annealing (SA) and direct-binary search (DBS) are traditional search algorithms which require less time to converge.[56,57] However, these two algorithms also easily fall into local optimal solution because they are sensitive to the initial states and optimization parameter settings. For specific inverse design tasks with different frameworks, the performance of these algorithms are very different. It is necessary to select the most suitable algorithm according to the actual performance.

In this paper, we propose a programmable plasmonic waveguide system (PPWS) based on MCMs and the inverse design to obtain several different functions. Four optimization algorithms, including GA, PSO, SA and DBS, are used to design for the MCMs in the PPWS to realize multiple optical filtering functions, such as narrowband band stop filter (NBSF), broadband band stop filter (BBSF), narrowband band pass filter (NBPF) and broadband band pass filter (BBPF). The numerical simulation results exhibit that the performance of filters is improved based on the inverse design and weighting operation. For instance, the bandwidth and quality factor of the optimized NBSF can reach 6.5 nm and 200.5, respectively. In addition, some relatively complex transmission characteristics can also be obtained by using the PPWS, for example single plasmon-induced transparency (PIT)-like effect, double PIT-like effects and wavelength-tunable PIT-like effects. In conclusion, GA is considered as the most efficient inverse design method for our system due to less optimization time and stable performance.

2 Device design and simulation results

As shown in Fig. 1(a), our proposed PPWS consists of a MDM waveguide and MCMs. The MDM waveguide and MCMs are placed on a SiO_2 substrate. Here, the MCMs whose footprint is 400×400 nm^2 and composition is $M \times N$ square pixels are placed on one side of the MDM waveguide. Each pixel in the MCMs can be selectively filled by Ag or

air, corresponding to the logical state "0" or "1", respectively. Obviously, MCMs provide a relatively broad programming space which is expected to realize different functions based on the inverse design technology. In the PPWS, the length and width of the MDM waveguide which transmits the transverse magnetic (TM) polarized light are 620 nm and 100 nm, respectively. The TM mode in the MDM waveguide can be coupled into the MCMs partially and then be coupled back into the MDM waveguide. The excited modes in the MCMs will have impact on the optical transmission characteristics in the transmission spectrum. In our simulations, the transmission spectrums are calculated by using the 2-dimensional (2D) finite-difference time-domain (FDTD) method (adopting Lumerical FDTD Solutions). The maximum mesh step is set as 1/4 of the length of single pixel in MCMs. The relative dielectric constant $\varepsilon(\omega)$ of the metal (Ag) in the FDTD simulation is modeled by the Drude model with $(\varepsilon_\infty, \omega_p, \gamma) = (3.7, 1.37 \times 10^{16} Hz, 2.7 \times 10^{13} Hz)$ by the following formula:[58]

$$\varepsilon(\omega) = \varepsilon_\infty - \frac{\omega_p^2}{\omega^2 + i\omega\gamma} \tag{1}$$

where ε_∞ is the interband-transition contribution to the permittivity, ω_p is the bulk plasma frequency, and γ is the electron collision frequency. The dispersion relation of the MDM in our system is governed by the following dispersion equation:

$$\tanh(\frac{d}{2}k_1) = -\frac{\varepsilon_1}{\varepsilon_2}\frac{k_2}{k_1} \tag{2}$$

where ε_1 and ε_2 are the relative dielectric constants of the dielectric and the metal, respectively. d is the width of the inner dielectric. k_1 and k_2 are the transverse propagation constants in the dielectric and the metal, respectively, which are related to the effective refractive index n_{eff} as:

$$k_i = \sqrt{n_{eff}^2 k_0^2 - \varepsilon_i^2 k_0^2}, (i = 1, 2) \tag{3}$$

The real part and imaginary part of n_{eff} theoretically calculated and numerically simu-
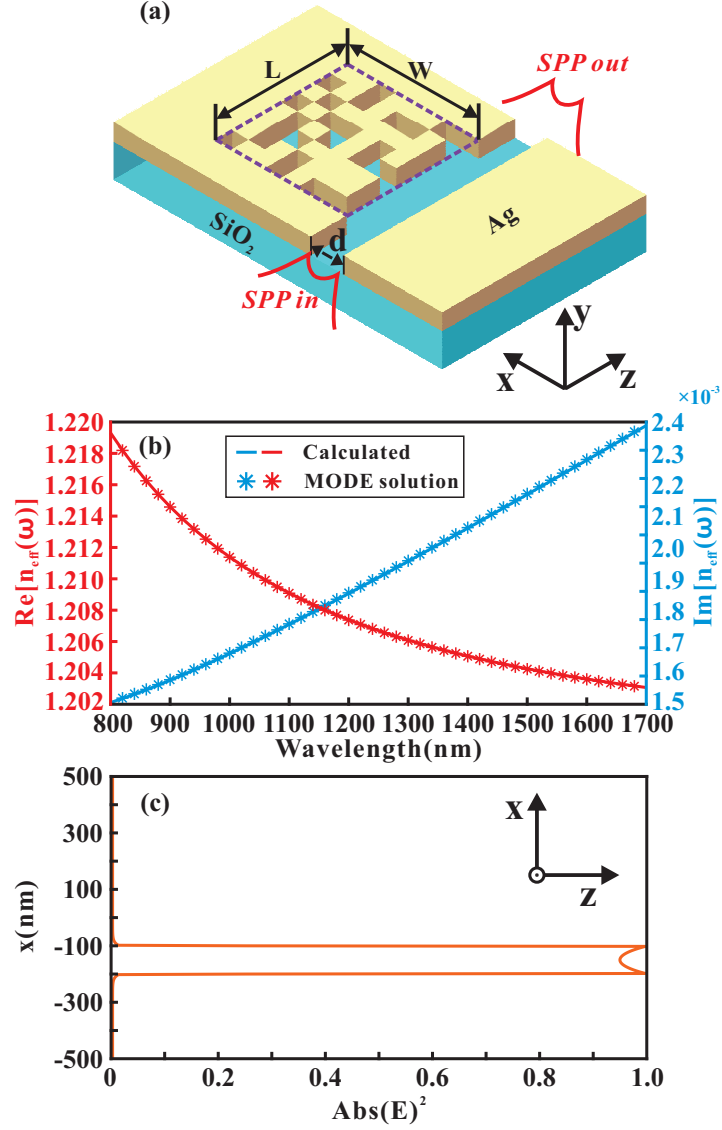
Figure 1: Structure schematic of the proposed PPWS, the effective refractive index and electric field intensity distribution in MDM. (a) The schematic of MDM waveguide and MCMs. (b) The real part (red) and imaginary part (blue) of n_{eff}. The solid lines represent the theoretical calculation results and star markers represent simulation results by MODE solution. (c) The electric field intensity distribution of TM mode in MDM.

lated by Lumerical MODE Solutions (which has the same solution in FDTD Solutions) are plotted in Fig. 1(b). The results show that our 2D FDTD simulations is in consistent with theory. Moreover, Fig. 1(c) exhibits the electric field intensity distribution of x direction in MDM which is a kind of symmetric TM mode. All the transmission spectrums in our simulations are calculated from 800 nm to 1700 nm in the near infrared region. It should be noted that the MDM waveguide system is usually simulated by using 2D FDTD simulation because of the less simulation time and high accuracy.[59–61] Although the 3D FDTD simulations are more close to the practical devices, their time consumption is relatively high.

As mentioned above, the PPWS provides a relatively broad programming space to support different functions. In practice, the MCMs can be dynamically controlled by using a field-programmable gate array.[38] Here, we randomly select several MCMs to exhibit the transmission characteristics of the PPWS, and the simulation results are shown in Fig. 2. In this simulation, the MCMs whose composition is 8×8 square pixels reveal that the PPWS has a programming space with 2^{64} distributions although some distributions are senseless and repetitive for one same objective. From Fig. 2(a-d), it can be observed that those transmission spectrums are expected to achieve multi-functional filtering, which is a fundamental and important unit in the integrated plasmonic circuits. And these transmission spectrums are simulated for the MCMs randomly selected from all possible distributions. Obviously, it indicates that the distribution of MCMs could greatly influence the output transmission spectrums and the performance metrics of these filters can be further improved based on the inverse design or optimization algorithms.

3 Multifunctional photonic device

3.1 Multifunctional filter

In section II, we have preliminarily proved that the PPWS has potential as multifunctional filters. It is expected to further improve the performance metrics of the filtering based on the
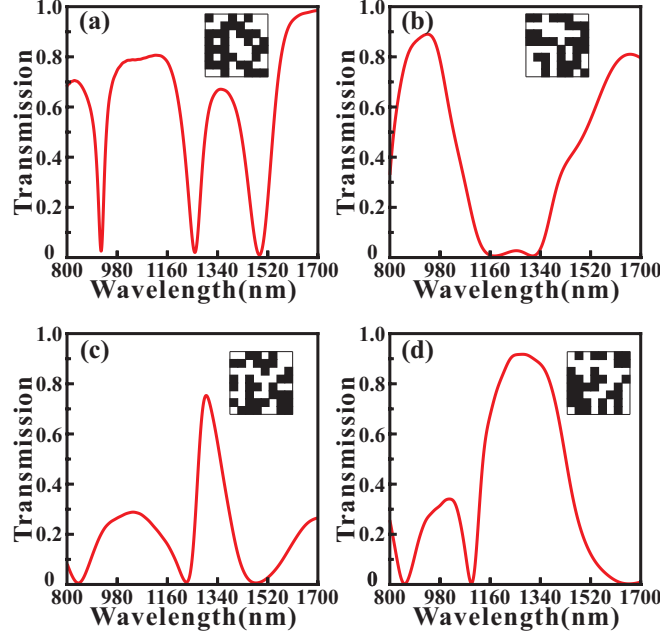
Figure 2: The simulated transmission spectrums for the MCMs with different distributions. (a) The transmission spectrum that is expected to be used as a NBSF. (b) The transmission spectrum that is expected to be used as a BBSF. (c) The transmission spectrum that is expected to be used as a NBPF. (d) The transmission spectrum that is expected to be used as a BBPF.

inverse design technology. For example, we want to design a NBSF whose central wavelength and 3dB bandwidth are 1300 nm and 20 nm, respectively. From the beginning, we randomly generate a number of MCMs whose transmission spectrums are simulated by using the 2D FDTD simulation. Then, the MCMs are optimized by using the GA, PSO, SA and DBS to achieve better performance, such as a narrower bandwidth. GA is a highly parallel and adaptive optimization algorithm, which encodes the solutions as genes to achieve evolutionary optimization. Because of the complexity of gene coding, the binary coding, which is suitable for our MCMs, is often used as a simplified substitution.[49] The algorithmic details of the GA used here are outlined as follows: (i) an initial population consisted of $N = 50$ individuals are randomly generated. Here, each individual in the initial population represents a distribution of MCMs whose pixels are randomly initialized as "0" or "1" state. It should be noted that N is an important parameter of the population which has influence on the convergence speed and optimization results. (ii) For all N MCMs, the transmission spec-

trums are calculated by using the 2D FDTD simulation. The Euclidean distance between the simulated transmission spectrum and the targeted transmission spectrum is defined as the optimization objective function (loss) for the GA. And it can determine whether one individual should be eliminated or not in the evolution. Furthermore, the setting of optimization objective function will be discussed in detail as a single part at the end of this section. (iii) A new population are generated by using the selection, crossover and mutation procedures. In the selection process, two parent individuals are selected from previous generation based on the roulette-wheel selection with a gap selection ratio of 0.9.[45] In the crossover process, the selected MCMs cross over to generate a new MCMs based on the uniform crossover method with a crossover probability of 0.3. In the mutation process, each pixel in the MCMs has 3% probability to flip from 0 (1) to 1 (0). (iv) The newly generated MCMs are evaluated to determine the GA whether to stop or not. If the genetic generation reaches to 100 or the value of optimization objective function remains unchanged for more than 30 times, then GA stops, otherwise, proceeds to Step (ii).

In comparison to GA, PSO is an evolution algorithm based on group cooperation, which is inspired from the foraging behavior of birds.[48] The solution (we call it "particle") of the optimization problem is a "bird" in the search space. All particles have a fitness value determined by the optimization objective function which is the same with GA, and each particle has a velocity that determines the direction and distance for their flight. It should be noticed that the standard PSO is suitable for the decimal problem rather than binary problem so that the discrete binary PSO (DBPSO) rather than the standard PSO is used to optimize the MCMs.[62] In the DBPSO, the calculation method for the velocity is as same as the standard PSO. But the velocity of the standard PSO directly affects the position of particle, while that of DBPSO is converted to a flip probability based on the sigmoid function.[63] Then, this flip probability determines whether the pixels in the MCMs are changed or not. It should be noted that the velocity range, inertia weight and acceleration constants of the DBPSO in the optimization are set as -1~1, 1, and $c_1 = c_2 = 1.49$,[64] respectively. SA is

a typical search algorithm which imitates the physical annealing in the quenching based on Monte Carlo iterative solution strategy.[65] At the initial stage, SA searches for the solution in a broad optimization space by accepting a worse solution with a certain probability. It can effectively alleviate the local optima problem in the GA and PSO to some extent.[66,67] As the temperature decreases, the solution changes in a small range to speed up the convergence of SA. Here, in each iteration, the MCMs are randomly generated and simulated by the 2D FDTD simulation. The objective function is evaluated to determine the newly generated MCMs whether to be accepted or not with an acceptance probability determined by the Metropolis criterion.[68] Here, the maximum and minimum of the temperature for the SA are set as 2000 and 1^{-18}, respectively. And the iteration times for the SA depend on the decrease rate (0.98) of temperature. In addition, DBS is a nonlinear search algorithm which is suitable for discrete binary image.[69] From the beginning, each pixel is traversed in turn, and the state with the smaller value of optimization objective function is selected and then fixed each time.[57] It should be noticed that the optimal solution will only approach to the direction of convergence in this selection process, so there will be no oscillation and rebound for the value of optimization objective function. Moreover, in order to enhance the performance of PPWS, we increase the time for traversing all pixels. In this article, if the traversal times of the DBS reaches to maximum or the value of loss remains unchanged for more than 10 times, then stopping the search.

We use GA, DBPSO, SA and DBS to optimize for the MCMs in the PPWS to achieve a NBSF for demonstrating the availability and effectiveness of optimization algorithms. Here, the MCMs in the PPWS are composed of 8×8 pixels. The targeted central wavelength of the NBSF is set as 1300 nm and the targeted full width at half maximum (FWHM) of the transmission dip is set as 20 nm. Here, the line shape of the targeted transmission spectrum is set as rectangle function. The targeted transmission spectrums (green dash lines) and the optimized transmission spectrums (red solid lines) are shown in Fig. 3. It can be found that the transmission spectrums have a notable improvement after optimizing

with four optimization methods since the optimized transmission spectrums are very close to the targeted transmission spectrums comparing with the initial transmission spectrums (blue dash line). Here, the initial transmission spectrums of the DBS and SA are calculated for the initial random distributions of the MCMs, while those of GA and DBPSO are the best individuals in the first generation. After optimizing, we can find that the minimum transmittances of the transmission dips are reduced to 0.0208, 0.0812, 0.1045 and 0.0184 for DBS, GA, DBPSO and SA, respectively. And the central wavelengths (FWHMs) of the optimized NBSFs are 1307.0 nm (7.5 nm), 1299.5 nm (7.5 nm), 1299.0 nm (10.5 nm) and 1303.0 nm (6.5 nm) for DBS, GA, DBPSO and SA, respectively. Correspondingly, the Q-factors of the optimized NBSFs can reach 174.27, 173.67, 123.71 and 200.46, respectively. Obviously, all optimization algorithms are convergent and effective because the optimized transmission spectrums are close to the targeted transmission spectrums. Even so, there exist slight performance differences of the fluctuation degree in the sideband of the optimized transmission spectrums. The max fluctuations of the sideband in the transmission spectrums optimized by the DBS, GA, DBPSO and SA are 2.28 dB, 1.32 dB, 1.48 dB and 0.64 dB, respectively. Though SA has the minimum transmittances and FWHM, which indicates it performs well in this simulation, it is unstable in the optimization process due to the sensitivity of initial condition. GA, by contrast, can get gratifying performance even if it only executes once or twice, which is more stable than others.

After the optimization, the distribution of the MCMs and the $Re(Hz)$ (real part) of the transmission characteristics for NBSF are shown in Fig. 4. The distribution of MCMs comes from the optimization results of DBS method in the Fig. 3. It can be found that for the transmission points at wavelengths 1100 nm and 1500 nm, the SPPs are slightly coupled into MCMs through the pixels surrounded by blue boxes. Obviously, it doesn't form a stable resonant mode so that SPPs pass through the MDM waveguide with low loss. For the transmission dip at 1300nm, the SPPs are coupled into the MCMs to form a strong resonant mode between the orange zone and magenta zone. Thus, an obvious transmission
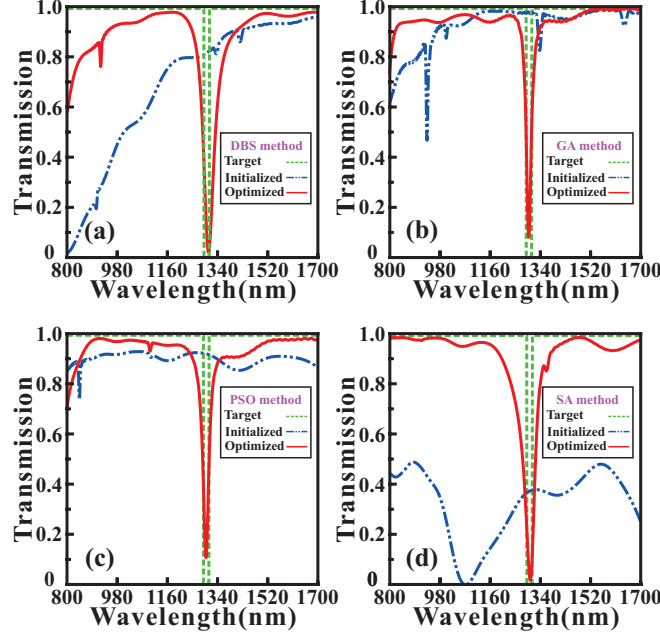
Figure 3: The initial transmission spectrums (blue dash lines) and optimized transmission spectrum (red solid lines) for (a) DBS, (b) GA, (c) DBPSO and (d) SA. The green dotted lines in (a), (b), (c) and (d) are the targeted transmission spectrums.

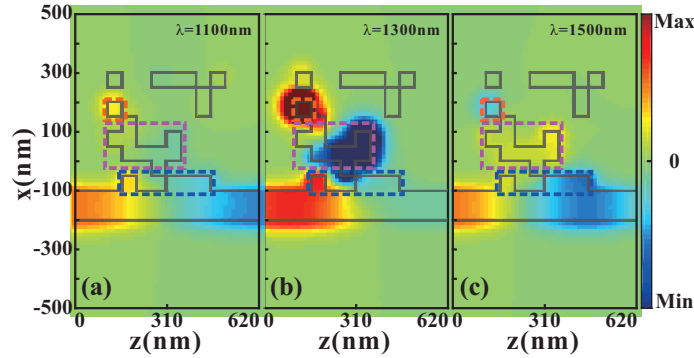dip emerges in the transmission spectrum.

Figure 4: The distribution of the MCMs and $Re(Hz)$ for the optimized NBSF at (a) 1100 nm, (b) 1300 nm, and (c) 1500 nm.

Then, we use GA to optimize for other three types of filters (BBSF, BBPF and NBPF), and corresponding simulation results are shown in Fig. 5. For contrast, the optimized results for the NBSF are shown in Fig. 5(a). Fig. 5(b) shows the optimized transmission spectrum for the BBSF, which has a wide stopband from 1100 nm to 1500 nm. It can be found that the transmittances are less than 0.01 in the stopband and higher than 0.8 in the passband,

indicating this BBSF can achieve promising filtering effects. In comparison to the NBSF, the stopband of the BBSF is not enough smooth. The reason for this phenomenon is attributed to the optimized MCMs have redundant pixels, which may lead to the deterioration of performance in the stopband. In addition, Fig. 5(c) shows the optimized transmission spectrum for the BBPF that has a broad passband from 1100 nm to 1500 nm. Here, the maximum transmittance and FWHM of the BBPF reach 0.9718 and 423 nm, respectively. And the maximum fluctuation degree in the passband of the BBPF is only 0.14 dB, which indicates that the passband is very flat. Moreover, we design a NBPF whose 3 dB bandwidth is 133.5 nm, and its optimized transmission spectrum is shown in Fig. 5(d). It can be observed that the maximum transmittance of the transmission peak can reach 0.8668 at 1296.5 nm. Obviously, the bandwidth and sideband inhibition of the NBPF cant be optimized as good as the NBSF. The reason for this phenomenon is related to the loss in the MCMs. In other words, the MCMs is easily used to inhibit rather than promote the transmission of specific wavelengths so that the NBSF have better performance than NBPF. In conclusion, the PPWS is demonstrated to be able to realize multiple optical filtering functions with the remarkable results. And we do not need to make any effort to analysis the resonant mode in the system ahead.

Next, two key elements which have significant influence on the optimal performance of filtering functions are discussed. Firstly, it is clear that the similarity between the simulated transmission spectrum and targeted transmission spectrum determines the performance after optimization. Here, we propose a simple but effective method named "weighting operation" to calculate the similarity for improving the performance metrics. As mentioned above, the Euclidean distances between the simulated transmission spectrums and targeted transmission spectrums are regarded as the optimization objective function (loss). Based on this, we use the weighting factor to calculate the Euclidean distance. The details are outlined as follows: (i) dividing the wavelength range of the transmission spectrums into two parts according to the importance. (ii) One part is called "The central wavelength range (TCWR)", which
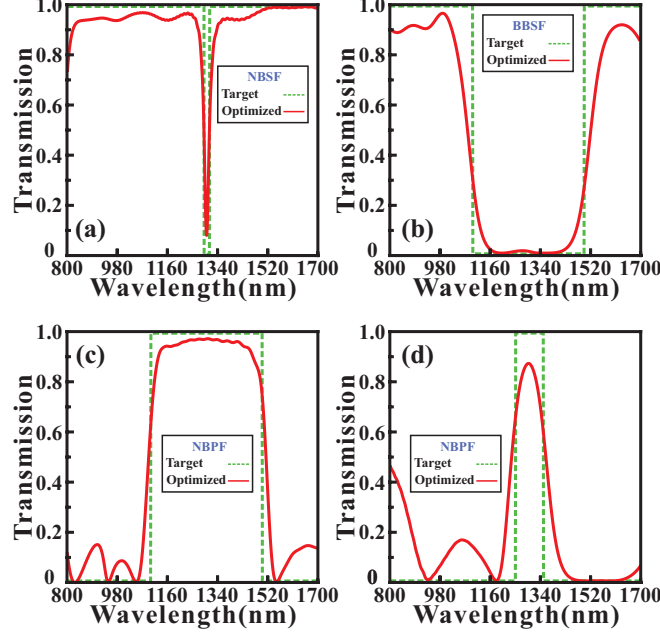
Figure 5: The transmission spectrums optimized by GA for (a) NBSF, (b) BBSF (c) BBPF and (d) NBPF. The green dotted line is the targeted transmission spectrum. Red solid line is the optimized transmission spectrum.

relates to the wavelength range of stopband or passband we focused on. The other is called "The else wavelength range (TEWR)", which has negligible influence on performance metrics. (iii) In each iteration, the loss L is calculated by the following formula:

$$L = w_{center} \times f(T^{sim}_{center} - T^{tar}_{center}) + w_{else} \times f(T^{sim}_{else} - T^{tar}_{else}) \tag{4}$$

where w_{center} is the weighting factor of TCWR, w_{else} is the weighting factor of TEWR. f is the function of calculating Euclidean distance. T^{sim}_{center} and T^{tar}_{center} represent the simulated transmission spectrum and targeted transmission spectrum in TCWR. While T^{sim}_{else} and T^{tar}_{else} are the simulated transmission spectrum and targeted transmission spectrum in TEWR.

In order to analyze the influence of the weighting operation, we use GA to optimize for the MCMs in the PPWS to achieve a NBSF. Here, the MCMs are composed of 8×8 pixels. The targeted central wavelength of the NBSF is set as 1300 nm and the FWHM of the transmission dip is set as 20 nm. TCWR includes the wavelength range from 1290 nm to 1310nm, and the rest of wavelength range belongs to TEWR. The optimized transmission

14

spectrums for different weighting factors w_{else} of TEWR are shown in Fig. 6(a). After the optimization, we find that the loss values with different weighting factors w_{else} have a significant decline in Fig. 6(b). The loss values decreases from 3.72 to 1.98 with a 46.77% decline ($w_{else} = 0.1$), 4.35 to 2.77 with a 36.32% decline ($w_{else} = 0.2$), 8.58 to 3.44 with a 59.91% decline ($w_{else} = 0.5$), 7.39 to 4.69 with a 36.54% decline ($w_{else} = 0.8$) and 14.69 to 6.14 with a 58.20% decline ($w_{else} = 1.0$), respectively. And the loss value has continuously decline with weighting factor w_{else} reducing, indicating that the weighting factor has a significant influence on the optimization effects. In Fig. 6(a), it can be found that the minimum transmittance at transmission dip is only 0.7968 when $w_{else} = 1.0$, which is still large for filter even if the loss value has a steep and quick decline in Fig. 6(b). As weighting factor w_{else} decreases, the minimum transmittance at transmission dip reduces to 0.2389, 0.0812, 0.0376 and 0.0360, respectively. However, it can be observed that the sideband has more violent fluctuations when w_{else} decreases from 1.0 to 0.1. Besides, the 3dB bandwidths are 14.5 nm, 7.5 nm, 10.5 nm and 8 nm for $w_{else} = 0.8$, $w_{else} = 0.5$, $w_{else} = 0.2$ and $w_{else} = 0.1$, respectively. As w_{else} decreases, the fluctuations in TEWR become more and more strong because the contribution of TEWR becomes smaller. At the same time, the significance of TCWR is amplified equivalently so a small transmittance at transmission dip can be achieved when w_{else} is decreased. In this article, we use a weighting factor of $w_{else} = 0.5$, which guarantees a balance between bandwidth, minimum transmittance and fluctuations of sideband. Obviously, it is better to dynamically adjust the weighting factor according to the specific application and optimization results of the PPWS.

The other key element for the optimization of the PPWS is the density of pixels in MCMs. Obviously, the diversity of MCMs determines the practical functions and performance of the PPWS. Mathematically, the permutation and combination of MCMs grows exponentially as the density of pixels in MCMs increasing. It should be noted that the optimization algorithms we used are suitable for global optimization task but their ability are not infinite. Therefore, it is necessary to choose an appropriate density of pixels in MCMs, which can
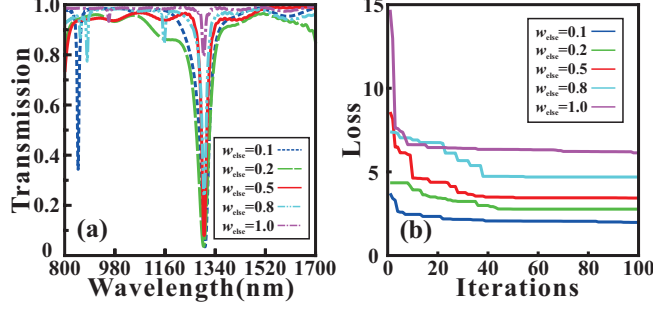
Figure 6: (a) The optimized transmission spectrums for the NBSF with different weighting factors w_{else}. (b) The variations of loss value for different weighting factors w_{else}. In all settings, w_{center} is set as 1.

not only ensure the diversity of MCMs but also maintain the efficiency of the optimization algorithms. In order to analyze the influence of density on the optimization performance, we use all algorithms to optimize for a NBSF with four different densities.

The targeted central wavelength of the NBSF is set as 1300 nm and the FWHM of the transmission dip is set as 20 nm. The optimized transmission spectrums of the NBSF with the MCMs whose densities are 5×5 pixels, 8×8 pixels, 10×10 pixels and 20×20 pixels are shown in Fig. 7(a)-(d), respectively. The important performance metrics of the optimized transmission spectrums for different densities are exhibited in Table 1. Here, T_{min} and L_c are the minimum transmittance and the central wavelength of the transmission dip. It can be found that T_{min} and 3dB bandwidth have remarkable declines as the density of MCMs increases. And the minimum transmittance and 3dB bandwidth for 20×20 pixels perform the worst in comparison to other densities. It can not be neglected that the fluctuations in the sideband for 20×20 pixels are extremely violent, which may restrict the applications of filtering function. The reason for this phenomenon is related to that the solution space of 20×20 pixels is too broad for optimization algorithm to search for the global optimal solution. In addition, it should be noted that the FDTD simulation for high-density MCMs will take much more time to converge as the computational complexity of the high-density MCMs is increased significantly. The choice of density for the MCMs depends on the practical requirements. Moreover, it can be found that the performance differences between 5×5

16

pixels, 8×8 pixels and 10×10 pixels are not obvious. In comparison to 5×5 pixels and 10×10 pixels, the inhibition of the sideband for 8×8 pixels performs better because it is smooth. The 3dB bandwidth and T_{min} for 5×5 pixels are more competitive, but the offset of central wavelength is relatively large, which limits the precise filtering. Considering the diversity and computational efficiency, we select the MCMs with 8×8 pixels to achieve most of the functionality in this article.
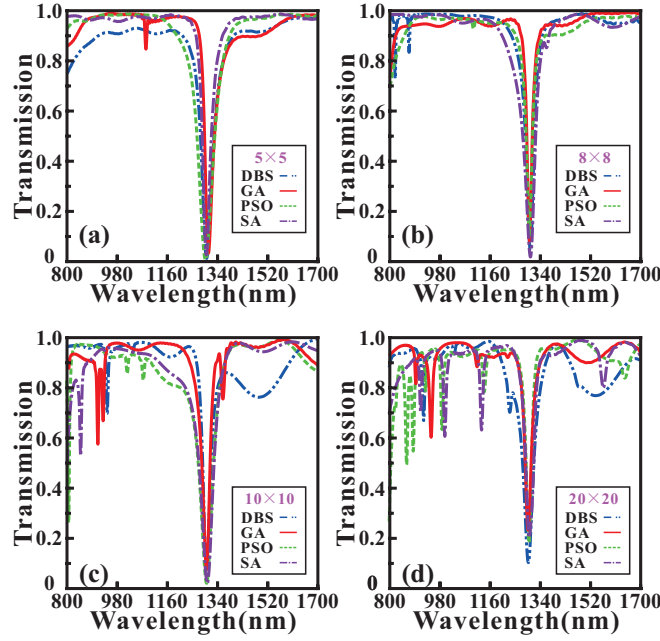

Figure 7: The optimized transmission spectrums of the NBSF with the MCMs whose densities are (a) 5×5 pixels (b) 8×8 pixels (c) 10×10 pixels (d) 20×20 pixels. Blue lines, red lines, green lines and purple lines are the transmission spectrums optimized by MDBS, GA, DBPSO, and SA, respectively.

3.2 PIT-like effect

In the previous section, we show that the PPWS can achieve a variety of filtering functions, but these functions are relatively simple. Actually, the PPWS can be programmed to realize advanced functions because of the diversity of MCMs. In addition, this programmable waveguide system can also be used to achieve wavelength-tunable optical devices based on optimization algorithms and the MCMs. Here, we use the GA, whose comprehensive

Table 1: Performance in different density of MCMs

Density	Method	L_c	T_{min}	3dB bandwidth
	DBS	1300.5	0.0124	6.0
	SA	1299.0	0.0267	6.5
5×5	DBPSO	1296.5	0.0071	6.0
	GA	1307.0	0.0330	7.0
	DBS	1302.5	0.0441	7.5
	SA	1303.0	0.0184	6.5
8×8	DBPSO	1299.0	0.1045	10.5
	GA	1299.5	0.0812	7.5
	DBS	1299.5	0.0657	9.5
	SA	1302.5	0.0185	8.0
10×10	DBPSO	1302.0	0.0206	8.5
	GA	1299.5	0.0737	10.0
	DBS	1299.5	0.1067	16.5
	SA	1302.5	0.2064	23.5
20×20	DBPSO	1301.5	0.1855	13.5
	GA	1298.5	0.2364	19.5

performance is the best in the previous section, to optimize for the MCMs to achieve the PIT-like effects in the transmission spectrum. The optical characteristic of the PIT-like effects includes a transmission peak located between two transmission dips, which has great applications in optical switches, optical data storage and slow light.[27,28] In this FDTD simulation, the MCMs are composed of 8×8 pixels. The targeted FWHM of the transmission peak is set as 20 nm, while the targeted FWHM of the whole transmission dip is set as 200 nm. The transmission spectrums optimized for the single PIT-like effect are shown in Fig. 8. Obviously, it can be observed that the single PIT-like effect whose center wavelength is 1297 nm is shown in Fig. 8(a), and the targeted central wavelength of the transmission peak is set as 1300 nm. The transmittance of the transmission peak reaches to 0.7115, while the transmittances of the transmission dips are 0.0084 (1251.5 nm) and 0.0086 (1333.5 nm), respectively. As a critical parameter to evaluate the performance of the PIT-like effect, the Q-factor, is calculated by the following formula:

$$Q = \frac{f_0}{FWHM} \tag{5}$$

18

where f_0 is the center wavelength of the single PIT-like effect. After the GA optimization, the $FWHM$ in Fig. 8(a) is 35.5 nm so that the Q-factor reaches to 36.54. In fact, the Q-factor is lower in the metallic systems due to the ohmic damping.[70] What's more, there is no need to analyze the complex coupling mechanism in a metallic resonator to achieve the single PIT-like effect. In our simulation, we just focus on using efficient optimization algorithms and reasonable physical conditions to obtain the targeted optical characteristics.
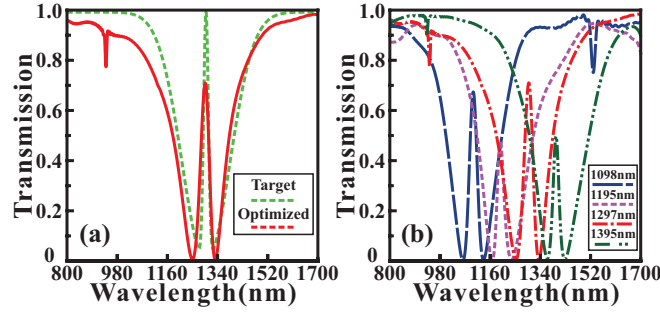

Figure 8: (a) The transmission spectrum optimized for a single PIT-like effect. The green dotted line is the targeted transmission spectrum. Red solid line is the optimized transmission spectrum. (b) Wavelength-tunable PIT-like effects with different central wavelength 1100 nm, 1200 nm, 1300 nm and 1400 nm.

In addition to the PIT-like effects at specific wavelength, the wavelength-tunable PIT-like effects are expected to be applied in highly integrated optical circuits due to flexibility.[71,72] For example, it has been demonstrated that the tunable PIT-like effects can be applied in optical modulators, switches, sensors, slow light and so on.[73] Fig. 8(b) shows the wavelength-tunable PIT-like effects based on the PPWS with different central wavelengths. In the optimization process, we only need to adjust the central position of the targeted PIT-like effects and keep other parameters fixed. The center (targeted) wavelengths of the tunable PIT-like effects are 1098 nm (1100 nm), 1195 nm (1200 nm) and 1395 nm (1400 nm), respectively. The maximum deviation between the center wavelength and targeted wavelength is only 5 nm. The corresponding FWHMs (Q-factors) of the tunable PIT- like effects are 31.5 nm (34.86), 27 nm (44.26) and 24 nm (58.13), respectively. And the extinction ratios between the transmission peak and two transmission dips are 22.53 dB (left) and 20.38 dB (right) for the PIT-like effect at 1098 nm, 20.52 dB (left) and 18.93 dB (right) for the PIT-like

19

effects at 1195 nm, 16.55 dB (left) and 18.22 dB (right) for the PIT-like effects at 1395 nm, respectively. Obviously, the FDTD simulation results show that the tunable PIT-like effects can be obtained in the wavelength range from 1100 nm to 1400 nm, which demonstrates that the PPWS has great flexibility and controllability based on the inverse design.
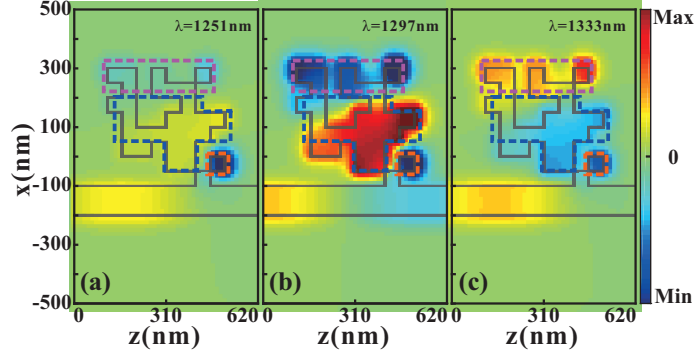

Figure 9: The distribution of the MCMs and PIT-like effects whose central wavelength is at 1297nm. The field distribution of $Re(Hz)$ at (a) 1251.5 nm, (b) 1297 nm, (c) 1333.5 nm.

For the single PIT-like effect, the distribution of the MCMs and corresponding electromagnetic field distributions are shown in Fig. 9. Based on the magnetic field distributions, we provide a qualitative explanation for the single PIT-like effect. It can be found that SPPs are confined in these regions which are marked by the yellow rectangular box and red rectangular box, leading to the transmission dips at 1251.5 nm and 1333.5 nm, respectively. For the transmission peak at 1297 nm, SPPs are coupled into yellow zone through the red zone to form a resonant mode. And the phase is same when SPPs are coupled back into the strip waveguide so there is a transmission peak. It should be noted that it is difficult to use the bright-dark mode coupling mechanism or doublet of dressed states to explain the PIT-like effects due to the irregular shapes of MCMs.[74]

Finally, we increase the complexity of the targeted transmission spectrum to achieve the double PIT-like effects. The simulated transmission spectrums are shown in Fig. 10. Here, Fig. 10(a) shows an ideal double PIT-like effects with higher transmittances, whose peaks reach to 0.7502 (left channel) and 0.7684 (right channel). By contrast, Fig. 10(b) shows the double PIT-like effects with lower transmittances in the transmission peaks. However,
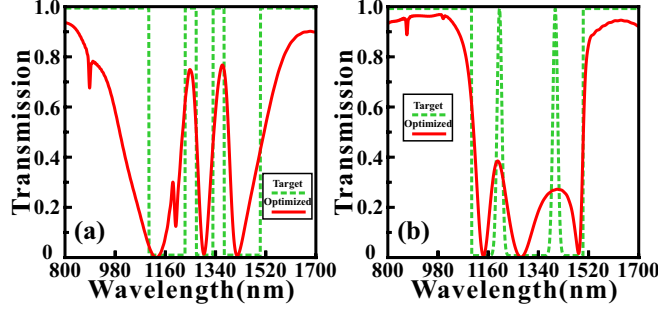
Figure 10: (a) The simulated transmission spectrums of the double PIT-like effects with higher transmittances. The targeted central wavelengths are set as 1250 nm and 1350nm. The targeted FWHMs of transmission peaks are both 40 nm. (b) The simulated transmission spectrums of the double PIT-like effects with lower transmittances. The targeted central wavelengths are set as 1200 nm and 1400 nm. The targeted FWHMs of transmission peaks are both 20 nm. The green dotted lines are the targeted transmission spectrums. The red solid lines are the simulated transmission spectrums.

the optimization and matching effects of sideband in Fig. 10(b) are better than those in Fig. 10(a). It should be noted that the sampling points in wavelength range are equidistant in our simulation. But the critical wavelength range that determines the optimization performance is relatively small. Although we use the weighting operation to eliminate the influence from sideband, there still are problems to be solved to make the simulation results match the targeted spectrums perfectly. Even so, it can be observed that the PPWS can be potentially applied to achieve more complex functions from Fig. 9 and Fig. 10.

4   Conclusion

In conclusion, we propose a PPWS based on MCMs and the inverse design. Several optimization algorithms, such as GA, SA, DBS and DBPSO are applied in the design of the MCMs to achieve different functions. The weighting operation can improve the optimization performance. And the FDTD simulation results demonstrate that the optimized PPWS can not only obtain simple functions (such as filters), but also achieve more complex transmission characteristics (for example single PIT-like effect, double PIT-like effects and wavelength-tunable PIT-like effects). Although the perfect matching between the targeted transmission

spectrum and optimized transmission spectrum is still difficult to achieve. These results indicate that the PPWS combined with the inverse design has great potential to realize multifunctional plasmonic devices with low cost and high efficiency. There is no need to spend much time on considering the shapes of resonators because the MCMs in the PPWS are re-programmable. In comparison to the previous works, our proposed PPWS not only provides a general framework for obtaining an effective, flexible and compact plasmonic device but also shows the applications of the inverse design on photonic devices.

Acknowledgement

References

(1) Cunningham, S.; Maradudin, A.; Wallis, R. Effect of a charge layer on the surface-plasmon-polariton dispersion curve. *Phys. Rev. B* **1974**, *10*, 3342–3355.

(2) Zayats, A. V.; Smolyaninov, I. I.; Maradudin, A. A. Nano-optics of surface plasmon polaritons. *Physics Reports* **2005**, *408*, 131–314.

(3) Hooper, I.; Sambles, J. Dispersion of surface plasmon polaritons on short-pitch metal gratings. *Phys. Rev. B* **2002**, *65*, 836–843.

(4) Otto, A. Excitation of nonradiative surface plasma waves in silver by the method of frustrated total reflection. *Z. Phys.* **1968**, *216*, 398–410.

(5) Kretschmann, E.; Raether, H. Notizen: Radiative Decay of Non Radiative Surface Plasmons Excited by Light. *Z. Naturforsch.* **1968**, *23*, 2135–2136.

(6) Lavers, C. R.; Wilkinson, J. S. A waveguide-coupled surface-plasmon sensor for an aqueous environment. *Sens. Actuators B Chem.* **1994**, *22*, 75–81.

(7) Stegeman, G. I.; Wallis, R. F.; Maradudin, A. A. Excitation of surface polaritons by end-fire coupling. *Opt. Lett.* **1983**, *8*, 386–388.

(8) Hecht, B.; Bielefeldt, H.; Novotny, L.; Inouye, Y.; Pohl, D. W. Local Excitation, Scattering, and Interference of Surface Plasmons. *Phys. Rev. Lett.* **1996**, *77*, 1889–1892.

(9) Kocabaş, Ş. E.; Veronis, G.; Miller, D. A. B.; Fan, S. Modal analysis and coupling in metal-insulator-metal waveguides. *Phys. Rev. B* **2009**, *79*, 035120.

(10) Du, B.; Yang, Y.; Zhang, Y.; Yang, D. Plasmonic Grating Based on Insulator-Metal-Insulator Structure at Telecom Wavelengths. *IEEE Photon. Technol. Lett.* **2018**, *30*, 1691–1694.

(11) Hua, L. U.; Gan, X.; Mao, D.; Zhao, J. Graphene-supported manipulation of surface plasmon polaritons in metallic nanowaveguides. *Photo. Res.* **2017**, *5*, 162–167.

(12) Lin, X.-S.; Huang, X.-G. Tooth-shaped plasmonic waveguide filters with nanometeric sizes. *Opt. Lett.* **2008**, *33*, 2874–2876.

(13) Lu, H.; Liu, X.; Mao, D.; Wang, L.; Gong, Y. Tunable band-pass plasmonic waveguide filters with nanodisk resonators. *Opt. Exp.* **2010**, *18*, 17922–17927.

(14) Kwon, M. S.; Shin, J. S.; Lee, J. H. Metal-Insulator-Silicon-Insulator-Metal Waveguide Splitters With Large-Arm Separation. *J. Lightw. Technol.* **2015**, *33*, 3843–3849.

(15) Yang, L.; Li, P.; Li, Z. Plasmonic polarization beam splitting based on single silver nanowire. *Opt. Exp.* **2019**, *27*, 3851–3860.

(16) Gómez-Díaz, J. S.; Perruisseau-Carrier, J. Graphene-based plasmonic switches at near infrared frequencies. *Opt. Exp.* **2013**, *21*, 15490–15504.

(17) Emboras, A.; Hoessbacher, C.; Haffner, C.; Heni, W.; Koch, U.; Ma, P.; Fedoryshyn, Y.; Niegemann, J.; Hafner, C.; Leuthold, J. Electrically Controlled Plasmonic Switches and Modulators. *IEEE J. Sel. Topics Quantum Electron.* **2015**, *21*, 1–8.

(18) Hoessbacher, C.; Josten, A.; Baeuerle, B.; Fedoryshyn, Y.; Leuthold, J. Plasmonic modulator with >170 GHz bandwidth demonstrated at 100 GBd NRZ. *Opt. Exp.* **2017**, *25*, 1762–1768.

(19) Zhang, B.; Zhao, Y.; Hao, Q.; Kiraly, B.; Khoo, I. C.; Chen, S.; Huang, T. J. Polarization-independent dual-band infrared perfect absorber based on a metal-dielectric-metal elliptical nanodisk array. *Opt. Exp.* **2011**, *19*, 15221–15228.

(20) Lu, H.; Liu, X.; Mao, D.; Wang, G. Plasmonic nanosensor based on Fano resonance in waveguide-coupled resonators. *Opt. Lett.* **2012**, *37*, 3780–3782.

(21) Ruoxi,; Yang,; Rami,; A.,; Wahsheh,; Zhaolin,; Lu,; Mustafa,; A.,; and, G. Efficient light coupling between dielectric slot waveguide and plasmonic slot waveguide. *Opt. Lett.* **2010**, *35*, 649–651.

(22) Virendra,; Patel,; Prateeksha,; Sharma,; V.,; Dinesh,; Kumar, Efficient Coupling From Dielectric to Hybrid Plasmonic Waveguide Using Curved Taper. *IEEE Photon. Technol. Lett.* **2019**, *31*, 323–326.

(23) Liu, Z.; Ding, L.; Yi, J.; Wei, Z.; Guo, J. Design of a multi-bits input optical logic device with high intensity contrast based on plasmonic waveguides structure. *Opt. Commun.* **2019**, *430*, 112–118.

(24) Zhang, H.; Shen, D.; Zhang, Y. Circular split-ring core resonators used in nanoscale metalinsulatormetal band-stop filters. *Laser Phys. Lett.* **2014**, *11*, 115902.

(25) Liu, X.; Tian, J.; Yang, R. Surface plasmon polariton based metal-insulator-metal filter including two face-to-face concentric semi-rings with different radii. *J. Opt. Technol.* **2017**, *84*, 588–592.

(26) Lai, W.; Wen, K.; Lin, J.; Guo, Z.; Hu, Q.; Fang, Y. Plasmonic filter and sensor based on a subwavelength end-coupled hexagonal resonator. *Appl. Opt.* **2018**, *57*, 6369–6374.

(27) Han, Z.; Bozhevolnyi, S. I. Plasmon-induced transparency with detuned ultracompact Fabry-Perot resonators in integrated plasmonic devices. *Opt. Exp.* **2011**, *19*, 3251–3257.

(28) Wang, G.; Lu, H.; Liu, X. Dispersionless slow light in MIM waveguide based on a plasmonic analogue of electromagnetically induced transparency. *Opt. Exp.* **2012**, *20*, 20902–20907.

(29) Zhan, S.; Li, H.; Cao, G.; He, Z.; Li, B.; Yang, H. Slow light based on plasmon-induced transparency in dual-ring resonator-coupled MDM waveguide system. *J. Phys. D, Appl. Phys.* **2014**, *47*, 205101.

(30) Chen, J.; Wang, C.; Zhang, R.; Xiao, J. Multiple plasmon-induced transparencies in coupled-resonator systems. *Opt. Lett.* **2012**, *37*, 5133–5135.

(31) Lu, H.; Liu, X.; Mao, D.; Gong, Y.; Wang, G. Induced transparency in nanoscale plasmonic resonator systems. *Opt. Lett.* **2011**, *36*, 3233–3235.

(32) Chen, H.; Zhang, H.; Guo, X.; Liu, S.; Zhang, Y. Tunable plasmon-induced transparency in H-shaped Dirac semimetal metamaterial. *Appl. Opt.* **2018**, *57*, 752–756.

(33) Han, X.; Wang, T.; Li, X.; Liu, B.; He, Y.; Tang, J. Ultrafast and Low-Power Dynamically Tunable Plasmon-Induced Transparencies in Compact Aperture-Coupled Rectangular Resonators. *J. Lightw. Technol.* **2015**, *33*, 3083–3090.

(34) Guo, J. Plasmon-induced transparency in metal-insulator-metal waveguide side-coupled with multiple cavities. *Appl. Opt.* **2014**, *53*, 1604–1609.

(35) Liu, H.; Ren, G.; Gao, Y.; Lian, Y.; Qi, Y.; Jian, S. Tunable subwavelength terahertz plasmon-induced transparency in the InSb slot waveguide side-coupled with two stub resonators. *Appl. Opt.* **2015**, *54*, 3918–3924.

(36) Lu, H.; Liu, X.; Mao, D. Plasmonic analog of electromagnetically induced transparency in multi-nanoresonator-coupled waveguide systems. *Phys. Rev. A* **2012**, *85*, 053803.

(37) He, Z.; Li, H.; Zhan, S.; Cao, G.; Li, B. Combined theoretical analysis for plasmon-induced transparency in waveguide systems. *Opt. Lett.* **2014**, *39*, 5543–5546.

(38) Cui, T. J.; Qi, M. Q.; Wan, X.; Zhao, J.; Cheng, Q. Coding metamaterials, digital metamaterials and programmable metamaterials. *Light Sci. Appl.* **2014**, *3*, e218.

(39) Jia, H.; Zhou, T.; Fu, X.; Ding, J.; Yang, L. Inverse-Design and Demonstration of Ultracompact Silicon Meta-Structure Mode Exchange Device. *Amer. Chem. Soc. Photon.* **2018**, *5*, 1833–1838.

(40) Shen, B.; Polson, R.; Menon, R. Broadband asymmetric light transmission via all-dielectric digital metasurfaces. *Opt. Exp.* **2015**, *23*, 20961–20970.

(41) Xie, Z.; Lei, T.; Qiu, H.; Zhang, Z.; Wang, H.; Yuan, X. Broadband on-chip photonic spin Hall element via inverse design. *Photo. Res.* **2020**, *8*, 121–126.

(42) Wang, K.; Ren, X.; Chang, W.; Lu, L.; Liu, D.; Zhang, M. Inverse design of digital nanophotonic devices using the adjoint method. *Photon. Res.* **2020**, *8*, 528–533.

(43) Molesky, S.; Lin, Z.; Piggott, A. Y.; Jin, W.; Vuckovic, J.; Rodriguez, A. W. Inverse design in nanophotonics. *Nature Photon.* **2018**, *12*, 659–670.

(44) Hughes, T. W.; Minkov, M.; Williamson, I. A. D.; Fan, S. Adjoint Method and Inverse Design for Nonlinear Nanophotonic Devices. *Amer. Chem. Soc. Photon.* **2018**, *5*, 4781–4787.

(45) Zhang, T.; Wang, J.; Liu, Q.; Zhou, J.; Dai, J.; Han, X.; Zhou, Y.; Xu, K. Efficient spectrum prediction and inverse design for plasmonic waveguide systems based on artificial neural networks. *Photo. Res.* **2019**, *7*, 368–380.

(46) Liu, D.; Tan, Y.; Khoram, E.; Yu, Z. Training Deep Neural Networks for the Inverse Design of Nanophotonic Structures. *Amer. Chem. Soc. Photon.* **2018**, *5*, 1365–1369.

(47) Holland, J. H. *Adaptation in Natural and Artificial Systems: An Introductory Analysis with Applications to Biology, Control, and Artificial Intelligence*; MIT Press, 1992.

(48) Kennedy, J.; Eberhart, R. C. Particle swarm optimization. **2002**, *4*, 1942–1948.

(49) Skaar, J.; Risvik, K. M. A genetic algorithm for the inverse problem in synthesis of fiber gratings. *J. Lightw. Technol.* **1998**, *16*, 1928–1932.

(50) Kern, D. J.; Werner, D. H. A genetic algorithm approach to the design of ultrathin electromagnetic bandgap absorbers. *Microw. Opt. Technol. Lett.* **2003**, *38*, 61–64.

(51) Chen, P.; Chen, C.; Wang, H.; Tsai, J. H.; Ni, W. Synthesis design of artificial magnetic metamaterials using a genetic algorithm. *Opt. Exp.* **2008**, *16*, 12806–12818.

(52) Zhang, T.; Xie, J.; Dan, Y.; Yu, S.; Han, X.; Dai, J.; Xu, K. Efficient Optical Spatial First-Order Differentiator Based on Graphene-Based Metalines and Evolutionary Algorithms. *IEEE Photon. J.* **2020**, *12*, 1–10.

(53) Shokoohsaremi, M.; Magnusson, R. Particle swarm optimization and its application to the design of diffraction grating filters. *Opt. Lett.* **2007**, *32*, 894–896.

(54) Forestiere, C.; Donelli, M.; Walsh, G. F.; Zeni, E.; Miano, G.; Dal Negro, L. Particle-swarm optimization of broadband nanoplasmonic arrays. *Opt. Lett.* **2010**, *35*, 133–135.

(55) Lu, Q.; Wei, W.; Yan, X.; Shen, B.; Luo, Y.; Zhang, X.; Ren, X. Particle swarm optimized ultra-compact polarization beam splitter on silicon-on-insulator. *Photon. Nanostr. Fundam. Appl.* **2018**, *32*, 19–23.

(56) Kim, W. J.; O'Brien, J. D. Optimization of a two-dimensional photonic-crystal waveguide branch by simulated annealing and the finite-element method. *J. Opt. Soc. Am. B* **2004**, *21*, 289–295.

(57) Shen, B.; Wang, P.; Polson, R.; Menon, R. An integrated-nanophotonics polarization beamsplitter with $2.4 \times 2.4~\mu m^2$ footprint. *Nature Photon.* **2015**, *9*, 378–382.

(58) Johnson, P. B.; Christy, R. W. Optical Constants of the Noble Metals. *Phys. Rev. B* **1972**, *6*, 4370–4379.

(59) Cao, G.; Li, H.; Zhan, S.; Xu, H.; Liu, Z.; He, Z.; Wang, Y. Formation and evolution mechanisms of plasmon-induced transparency in MDM waveguide with two stub resonators. *Opt. Exp.* **2013**, *21*, 9198–9205.

(60) Zhan, S.; Peng, Y.; He, Z.; Li, B.; Chen, Z.; Xu, H.; Li, H. Tunable nanoplasmonic sensor based on the asymmetric degree of Fano resonance in MDM waveguide. *Sci. Rep.* **2016**, *6*, 22428–22428.

(61) Pannipitiya, A.; Rukhlenko, I. D.; Premaratne, M.; Hattori, H. T.; Agrawal, G. P. Improved transmission model for metal-dielectric-metal plasmonic waveguides with stub structure. *Opt. Exp.* **2010**, *18*, 6191–6204.

(62) Kennedy, J.; Eberhart, R. C. A discrete binary version of the particle swarm algorithm. **1997**, *5*, 4104–4108.

(63) Chuang, L.; Chang, H.; Tu, C.; Yang, C. Improved binary PSO for feature selection using gene expression data. *Comput. Biol. Chem.* **2008**, *32*, 29–38.

(64) Eberhart, R. C.; Shi, Y. Comparing inertia weights and constriction factors in particle swarm optimization. **2000**, *1*, 84–88.

(65) Laarhoven, P. J. M.; Aarts, E. H. L. *Simulated Annealing: Theory and Applications*; Kluwer Academic Publishers: USA, 1987.

(66) Jamili, A.; Shafia, M. A.; Tavakkolimoghaddam, R. A hybrid algorithm based on particle swarm optimization and simulated annealing for a periodic job shop scheduling problem. *J. Adv. Manuf. Technol.* **2011**, *54*, 309–322.

(67) Yu, H.; Fang, H.; Yao, P.; Yuan, Y. A combined genetic algorithm:simulated annealing algorithm for large scale system energy integration. *Comput. Chem. Eng.* **2000**, *24*, 2023–2035.

(68) Kirkpatrick, S.; Gelatt, C. D.; Vecchi, M. P. Optimization by Simulated Annealing. *Science* **1983**, *220*, 671–680.

(69) Seldowitz, M. A.; Allebach, J. P.; Sweeney, D. W. Synthesis of digital holograms by direct binary search. *Appl. Opt.* **1987**, *26*, 2788–2798.

(70) Hu, J.; Lang, T.; Hong, Z.; Shen, C.; Shi, G. Comparison of Electromagnetically Induced Transparency Performance in Metallic and All-Dielectric Metamaterials. *J. Lightw. Technol.* **2018**, *36*, 2083–2093.

(71) Han, X.; Wang, T.; Li, X.; Xiao, S.; Zhu, Y. Dynamically tunable plasmon induced transparency in a graphene-based nanoribbon waveguide coupled with graphene rectangular resonators structure on sapphire substrate. *Opt. Exp.* **2015**, *23*, 31945–31955.

(72) Zhang, T.; Dai, J.; Dai, Y.; Fan, Y.; Han, X.; Li, J.; Yin, F.; Zhou, Y.; Xu, K. Tunable Plasmon Induced Transparency in a Metallodielectric Grating Coupled With Graphene Metamaterials. *J. Lightw. Technol.* **2017**, *35*, 5142–5149.

(73) Wang, G.; Zhang, W.; Gong, Y.; Liang, J. Tunable Slow Light Based on Plasmon-Induced Transparency in Dual-Stub-Coupled Waveguide. *IEEE Photon. Technol. Lett.* **2015**, *27*, 89–92.

(74) Wang, T.; Zhang, Y.; Hong, Z.; Han, Z. Analogue of electromagnetically induced trans-

parency in integrated plasmonics with radiative and subradiant resonators. *Opt. Exp.* **2014**, *22*, 21529–21534.
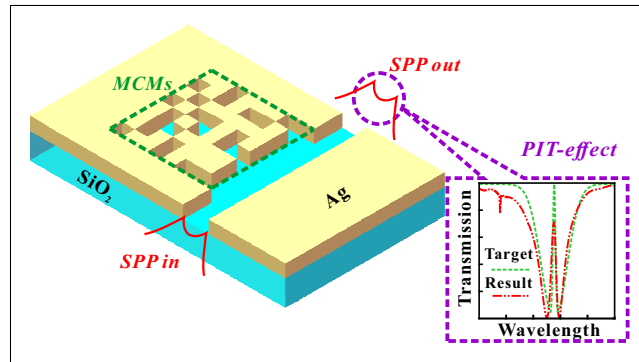
Graphical TOC Entry

Table of Contents Entry for *Programmable Multifunctional Plasmonic Waveguide System based on Coding Metamaterials and Inverse Design* by Yihang Dan, Tian Zhang, Jian Dai, and Kun Xu. Plasmon-induced transparency-like effect in a metal-dielectric-metal waveguide system is realized based on metal coding metamaterials and inverse design. The metal coding metamaterials marked with green dotted line is optimized by gradient free methods.